



JGR Solid Earth

RESEARCH ARTICLE

10.1029/2018JB016167

Key Points:

- Autocorrelation of local earthquake coda successfully images the subducting crust in Alaska
- Results provide higher-resolution imaging than receiver functions
- When combined with a dense network, autocorrelation of local earthquake coda could use high frequencies for detailed imaging

Supporting Information:

- Supporting Information S1
- Table S1

Correspondence to:

D. Kim,
dk696@cornell.edu

Citation:

Kim, D., Keranen, K. M., Abers, G. A., & Brown, L. D. (2019). Enhanced resolution of the subducting plate interface in Central Alaska from autocorrelation of local earthquake coda. *Journal of Geophysical Research: Solid Earth*, 124, 1583–1600. <https://doi.org/10.1029/2018JB016167>

Received 1 JUN 2018

Accepted 22 DEC 2018

Accepted article online 29 DEC 2018

Published online 5 FEB 2019

Enhanced Resolution of the Subducting Plate Interface in Central Alaska From Autocorrelation of Local Earthquake Coda

Doyeon Kim¹ , Katie M. Keranen¹, Geoffrey A. Abers¹, and Larry D. Brown¹

¹Earth and Atmospheric Sciences, Cornell University, Ithaca, NY, USA

Abstract Subducting plates below 10-km depth are primarily imaged using phases from teleseismic earthquakes at frequencies dominantly below 1 Hz, resulting in low-resolution images compared to fault zone thickness. Here we image the plate boundary zone in Alaska using scattered body wave arrivals in local earthquake coda to produce a higher-resolution image of the slab. An autocorrelation method successfully extracts coherent arrivals from the local earthquake signals. Our autocorrelation results image interfaces associated with the subducting oceanic plate at higher resolution than our teleseismic receiver functions, with increased coherence and sharper boundaries. Our results provide one of the first coherent structural images of the seismogenic zone using scattered local body waves. Amplitudes suggest that seismic wave speed decreases with increasing depth within the low-velocity zone, supporting lithologic rather than purely overpressure models for the zone in our region. Similar methodologies using dense stations could provide higher-resolution images to characterize crustal and uppermost mantle boundaries globally.

1. Introduction

The physical properties of subduction interfaces at convergent plate boundaries impact megathrust seismicity and arc volcanism but remain incompletely understood. Key questions remain regarding the physical properties and processes that control rupture initiation, propagation and termination (Dixon & Moore, 2007). Improving the resolution of seismic imaging at depths of several tens of kilometers could significantly advance our understanding of plate boundaries, including the width of the plate boundary and its internal physical properties.

Seismic images of the subduction interface are commonly created using teleseismic conversions from boundaries, often computed as receiver functions (RFs; e.g., Burdick & Langston, 1977). RFs in Alaska delineate the subducted plate and the upper plate (e.g., Ferris et al., 2003; Kim et al., 2014) and indicate a 2- to 5-km-thick low-velocity zone (LVZ) at the top of subducting crust at depths where great earthquakes rupture (Ichinose et al., 2007). RFs in northern Cascadia also indicate a LVZ, 3.4 ± 1.0 km thick with high Vp/Vs ratios (>2.0) immediately above subducting crust (Audet et al., 2009; Hansen et al., 2012), interpreted as an overpressured channel at the subducting plate interface. RF images elsewhere show subducting crust as a low-velocity layer but do not always resolve an overlying LVZ (see compilation of Bostock, 2013). Teleseismic P wave energy used in these studies is dominantly at frequencies <1 Hz with corresponding effective sampling wavelengths >5 –10 km (following the analysis of MacKenzie et al., 2010), so RFs are not capable of resolving <1 -km-thick layers such as those imaged near the plate interface with active source data (e.g., Li et al., 2015) or observed in exhumed megathrusts (Rowe et al., 2013). Even using free surface multiples, with improved resolution by a factor of 3–5 (Rondenay, 2009), typical RF signals still cannot resolve structures smaller than ~ 2 km. Other methods to image slabs such as local earthquake tomography (e.g., Kato et al., 2010; Tsuji et al., 2008) are further limited in resolution such that features smaller than ~ 10 km are rarely resolved even with dense networks, with similar limitations for waveform modeling (e.g., Song et al., 2009). Given these limitations, local earthquake sources with energy at frequencies from the microseismic noise band (0.06–0.2 Hz) to ~ 10 Hz, and with greater energy than active sources, provide a potential means to image small-scale slab structure at high resolution.

In this study we use autocorrelation of local earthquake coda from central Alaska (Figure 1) to show that reflected and converted seismic waves are capable of mapping subducting slab structure. Our results

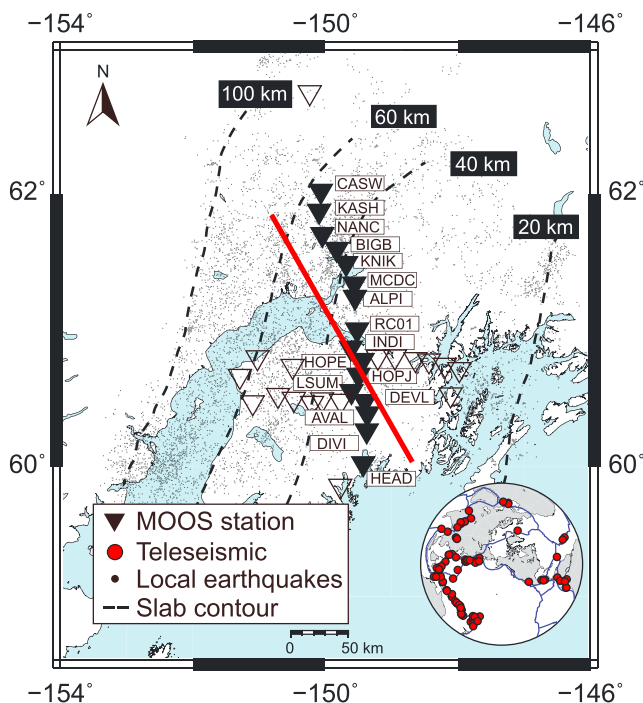


Figure 1. Study area in the Alaska-Aleutian subduction zone. Multidisciplinary Observations Of Subduction (MOOS) seismic stations (Li et al., 2013) are inverted triangles; data from stations with solid black symbols are used in this study. Local seismicity from 2007 to 2008 (black dots) and inferred depth contours of the top of the subducting slab (dashed black lines) are from the relocated catalog of Li et al. (2013). Data are projected onto a 2-D transect parallel to the subduction direction (red line). Red circles in the inset map are teleseismic earthquakes used in receiver functions.

contain higher resolution than RFs at the same stations and provide better resolution than many other seismic interferometric studies in subduction zones (e.g., Ito & Shiomi, 2012; Nishitsuji et al., 2016; Ruigrok & Wapenaar, 2012). Our higher-resolution imaging of the subducting Yakutat crust in central Alaska with local earthquake coda begins to bridge the gap toward features at the scale of damage zones along plate boundary faults. Synthetic data demonstrate that the autocorrelation method with data from dense arrays could image the structure of subsurface interfaces with frequencies of ~ 10 Hz, approaching the resolution obtained using active source methods at these depths.

2. Background

In recent years, methods of seismic interferometry have developed that cross-correlate seismic traces between two stations. Such studies now routinely extract surface waves from ambient microseismic noise (e.g., Lin et al., 2008; Shapiro et al., 2005). Interferometry has also been applied in attempts to extract body waves from ambient noise (e.g., Draganov et al., 2009; Lin et al., 2013; Roux et al., 2005; Ryberg, 2011; Zhan et al., 2010), from discrete sources including in exploration seismology (e.g., Schuster, 2009; Wapenaar et al., 2008) and from local or teleseismic earthquake signals (e.g., Kim et al., 2017; Nakata et al., 2014; Ruigrok & Wapenaar, 2012). However, distinct boundaries have commonly been difficult to image in the body waves from these studies, particularly at depths of more than a few kilometers, so the method is not commonly used for such imaging. These methods have been applied in subduction zones, using cross correlation between station pairs using regional earthquakes (Nishitsuji et al., 2016), teleseismic earthquakes (Ruigrok & Wapenaar, 2012), or ambient noise (Ito & Shiomi, 2012); the results of these studies have been challenging to interpret.

3. Data

We use seismic data from 16 stations within the MOOS (Multidisciplinary Observations Of Subduction) network (Li et al., 2013) and station RC01 from the Alaska permanent network (Alaska Earthquake Center, 1987; Figure 1). These stations form an irregular transect which, when projected down-dip (30° west of north) sample the subducting slab at ~ 10 - to 15-km spacing from 25- to 60-km depth (Figures 1 and 2). A shorter E-W cross line exists (open symbols, Figure 1) but was not used due to its lower data quality (Kim et al., 2014). MOOS data were acquired with broadband seismometers sampled at 50 samples per second, here analyzed for 13 months from August 2007 to August 2008. Local and teleseismic earthquakes recorded by stations on this transect are used for autocorrelation and RF analyses, respectively. We also calculated autocorrelations of ambient noise for comparison, using windows without earthquakes.

We use local earthquake hypocenters from the double-difference catalog and velocity model of Li et al. (2013). We subset the catalog to 1,196 of 8,308 earthquakes by choosing events with epicenters within 20 km of a station (Table S1 in the supporting information). Earthquakes in our final analysis are restricted to near-vertical raypaths, within a horizontal earthquake-station distance to earthquake depth ratio of 0.5 (or in a 22.5° wide cone with apex at the station). We further subset the earthquakes based on the quality of the autocorrelation result, using 607 earthquakes in our final result (Tables S1 and S2), ranging in depth from 14 to 72 km (Figure S1). Magnitudes (M_L) range from 0.1 to 5.4 (Li et al., 2013). Local earthquakes have energy up to 10 Hz (Figure 3). Signal-to-noise ratio (SNR) is below 1 at frequencies less than ~ 0.5 Hz for most events (Figure 3). For RFs, we selected teleseismic earthquakes of magnitude greater than M_b 6.0 within epicentral distances of 30° to 90° , a total of 80 earthquakes (inset, Figure 1).

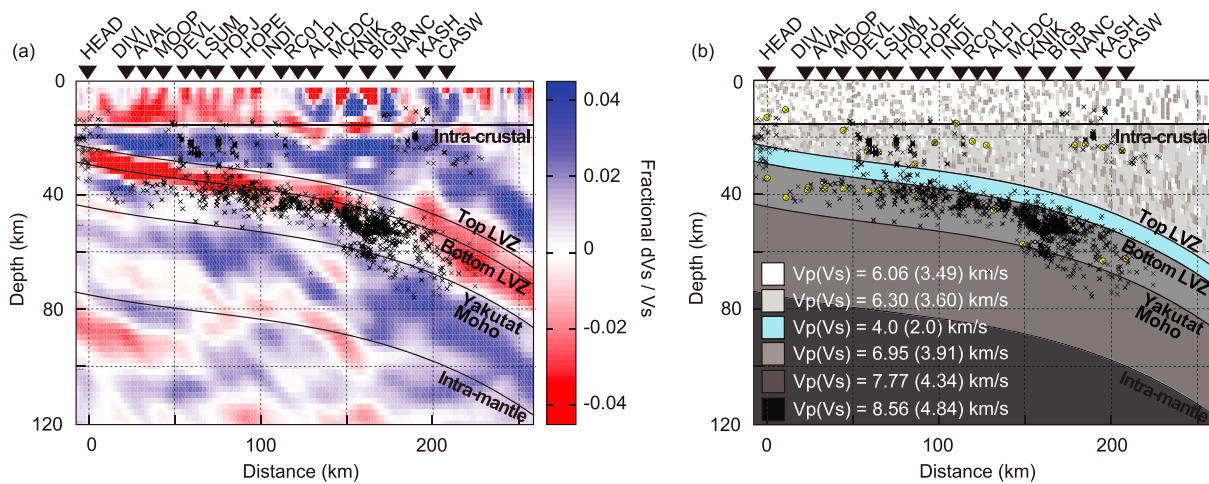


Figure 2. (a) A portion of the receiver function migration image (Kim et al., 2014) used to determine the location of the primary boundaries in our forward model of subducting slab structure. The colors on the image represent the magnitude and polarity of the velocity perturbations (in fractional dV_s/V_s) required to produce the observed scattered wavefield. The inversion result is derived from a 2-D generalized radon transform inversion. Zero distance is at station HEAD. (b) Velocity model used in our synthetic modeling, based on the image in (a) for structural boundaries and on the results of the travel time inversion of Li et al. (2013) for the seismic velocity of each layer. The LVZ (blue) was added based on receiver function modeling results from Kim et al. (2014). Local earthquakes (black symbols) are from within 20 km of the best fit line to the Multidisciplinary Observations Of Subduction stations, projected onto the model. Earthquakes used in synthetic modeling are denoted by yellow circles. The model includes random scatterers in the upper crustal layer of $\pm 5\%$ (e.g., Frankel & Clayton, 1986) to generate earthquake coda energy. LVZ = low-velocity zone.

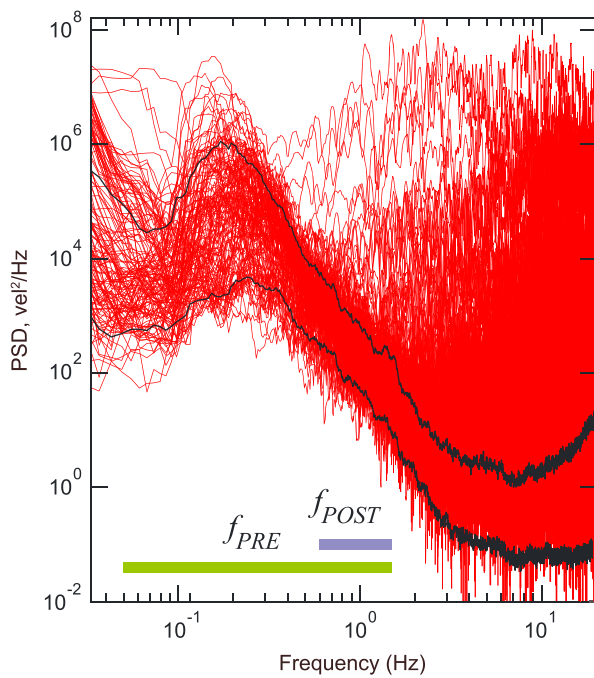


Figure 3. Power spectra for earthquakes from station HOPE (red lines) and central 75% of corresponding preevent noise (black lines). Color bars show frequency bands used in prestack (f_{PRE}) and poststack (f_{POST}) filtering of autocorrelation images, as described in text. Few earthquakes have signal-to-noise ratio much above 1 at frequencies < 1 Hz. PSD = power spectral density.

4. Methods

4.1. Autocorrelation of Local Earthquake Recordings From MOOS Data

Local earthquakes provide discrete sources of energy and create direct arrivals and reflections, conversions, and reverberations from subsurface boundaries either above or below the source (Figure 4). The timing of reverberations within the earthquake coda is a function of boundary depth, incidence angle, and seismic wave speed, as in surface seismic reflection data, and thus contain similar information on subsurface boundary structure (e.g., Claerbout, 1968). The reverberations are weak in amplitude, and coherent signals are masked by noise. In methods utilizing weak reflection energy, multiple traces are commonly summed (stacked) to increase SNR. However, variability in earthquake location and depth, and variable source signatures, precludes direct stacking of local earthquake traces because arrival times and polarities vary (Figure 5). Autocorrelation of local earthquake data facilitates stacking by removing the effects of varying source mechanisms and by aligning traces on the direct arrival from each source, effectively removing the moveout for the direct arrival (Figures 5 and 6). This alignment on the direct arrival also aligns later reverberatory arrivals, with minor residual moveout (Figures 5 and 6). Stacking autocorrelation traces for near-vertical raypaths thus constructively sums surface reflections from subsurface boundaries, creating “virtual sources” from the underside of the free surface to subsurface reflectors (Figure 4).

In our methodology, we use the autocorrelation of the direct arrivals with reverberations within the coda. We consider the coda to include the first several reverberations of body waves from the subducting slab. In this

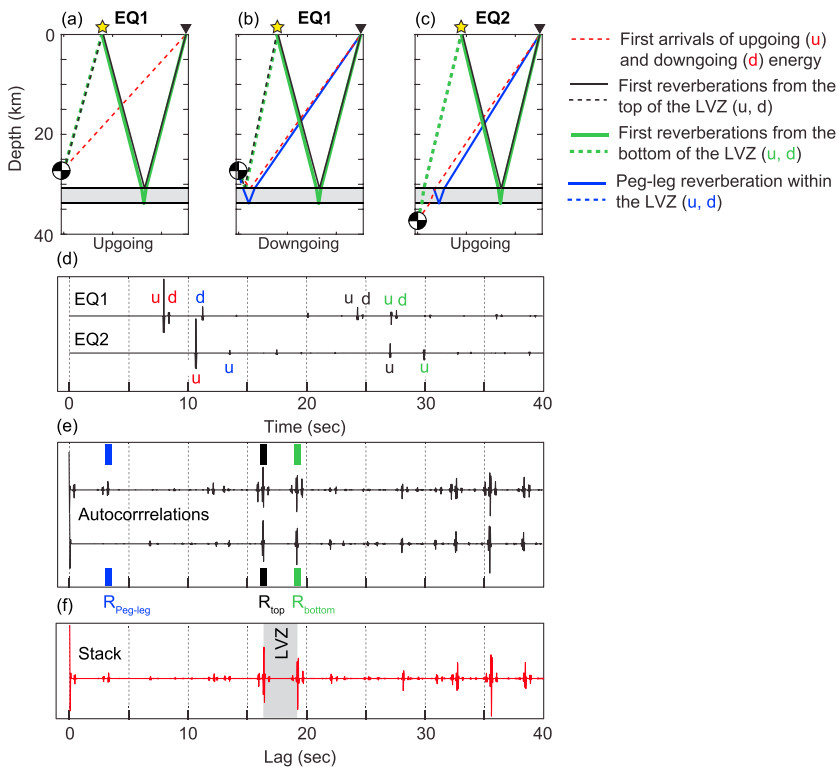


Figure 4. Schematic cartoon of the autocorrelation imaging method. (a–c) Upgoing and downgoing raypaths from earthquakes above (a, b) and below (c) the modeled low-velocity zone (LVZ) and synthetic waveforms (d). Only the first reverberations are shown for clarity, though multiple reverberations within each layer are present in the data and used in our analysis. Dashed lines represent ray segments with arrival times dependent upon source depth. Solid lines represent ray segments that are independent of source depth. These depth-independent segments are aligned after autocorrelation for near-vertical raypaths ($R_{\text{peg-leg}}$, R_{top} , and R_{bottom} in e). Rays used in our autocorrelation analysis are near-vertical; horizontal scale is expanded here for clarity. Beach ball shows earthquake source location, inverted triangle shows receiver, and star shows surface reflection point (virtual source). (d) Synthetic seismograms for these two earthquakes; upgoing and downgoing arrivals for raypaths in (a)–(c) are labeled. (e) Autocorrelation of traces in (d) aligns traces to zero lag at the direct arrival, with peaks at the delay times corresponding to pairs of arrivals. (f) Stack of traces in (e). The stack enhances common arrivals between earthquakes, including the surface reflections. The time interval between arrivals from the top and bottom of the LVZ is shaded gray and labeled. Effects of source mechanism and offset (moveout) are shown in Figures 5 and 6.

paper, we use the term “coda” because most of the information is derived from the later arrivals, though we recognize that strictly speaking our processing windows include the direct arrivals.

To create autocorrelation traces of local earthquakes in our study (processing flow in Table S3), we extract traces beginning 20 s before and ending 100 s after the predicted P arrival for each selected earthquake at each station. This time window encompasses the direct P and S waves and the first few reverberations from the boundaries of interest above and below the subducting crust. We rotate the horizontal components to radial and transverse polarization and apply the free surface transformation to rotate to P , SV , and SH components (Kennett, 1991). Prior to autocorrelation, the mean and the trend are removed from each trace and preautocorrelation and postautocorrelation band-pass filters are applied.

The 120-s-long traces from each earthquake-station combination are autocorrelated to lags of 60 s. Following autocorrelation, the traces were visually inspected at each station to eliminate those dominated by ringing of the autocorrelation or other noise, and we retained between 15 to 100% of traces (Table S1) for further processing. After application of the postprocessing 0.6- to 1.5-Hz filter, we apply an automatic-gain-control function with a time window of 8.0 s to increase the relative amplitude of later phases. Before stacking, we discard all autocorrelation traces with distance-to-depth ratios greater than 0.5 (Table S1), thus retaining those within a cone of 22.5° beneath the station, which have near-vertical incidence. We also tested wider

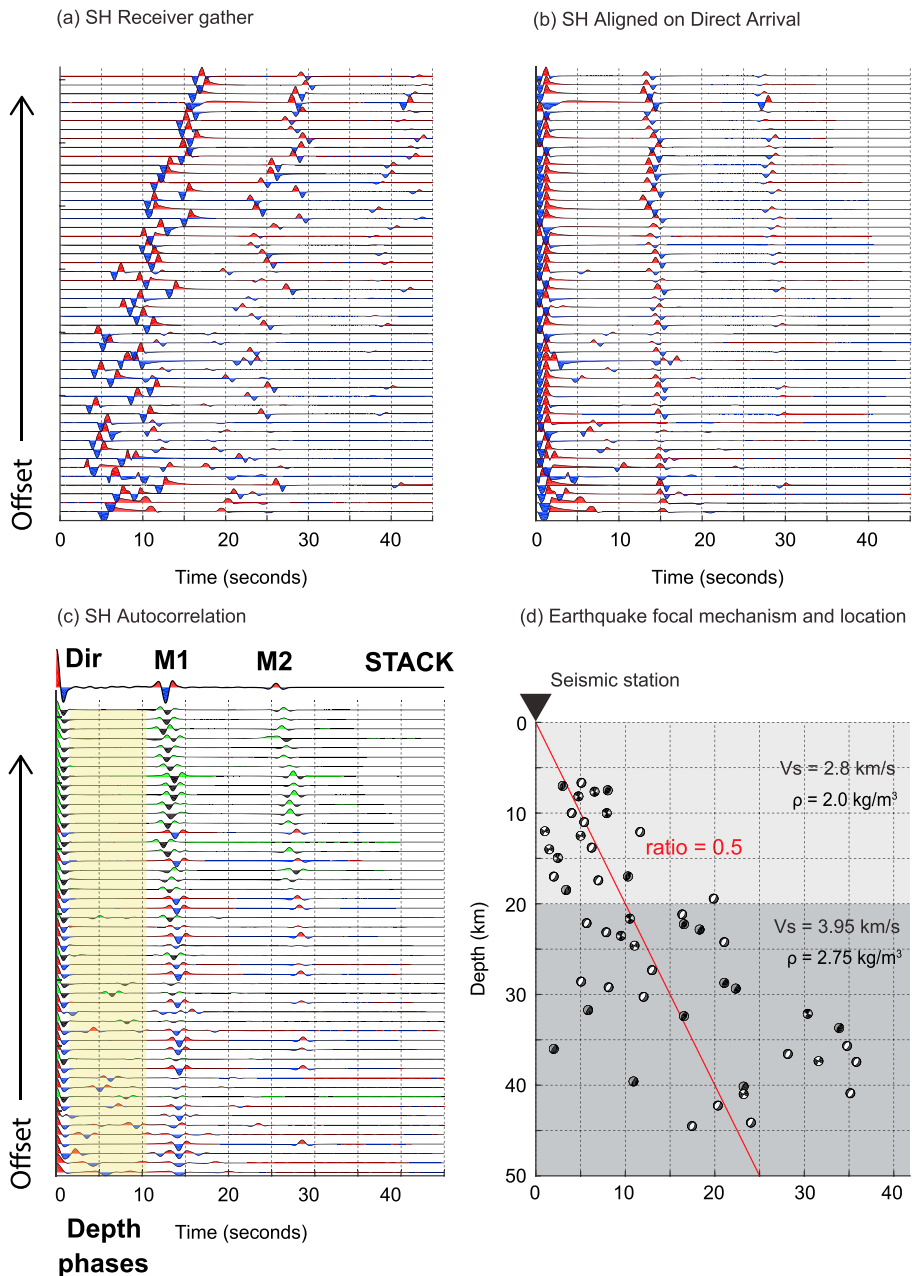


Figure 5. (a) Synthetic earthquakes and reverberations from a single horizontal boundary, calculated using codes from Herrmann (2013). Polarity of the direct arrival depends upon the earthquake focal mechanism and location (shown d). (b) Waveforms aligned on the direct arrival. Polarity of the direct arrival and polarity of the first multiple vary from trace to trace. (c) Autocorrelation traces of earthquakes in (a). Traces colored in green-black are beyond the angle ratio of 0.5. The first and secondary multiples are labeled as M1 and M2, respectively. Direct arrivals (at zero lag) are consistently positive, and the first multiple is consistently negative for earthquakes below the angle ratio of 0.5. These traces can be stacked to constructively sum energy in reverberations. Arrivals coming in before the first multiple on (c) (yellow shading) are “depth phases,” resulting from the autocorrelation of the upgoing direct arrival with the downgoing reflection from the boundary. The timing of this arrival depends upon source depth and is not consistent across all earthquakes; thus, the depth phases are suppressed in the stacked trace. A subset of earthquakes above the angle ratio of 0.5 is flipped in polarity as angles increase and the sign of the reflection coefficient flips. LVZ = low-velocity zone.

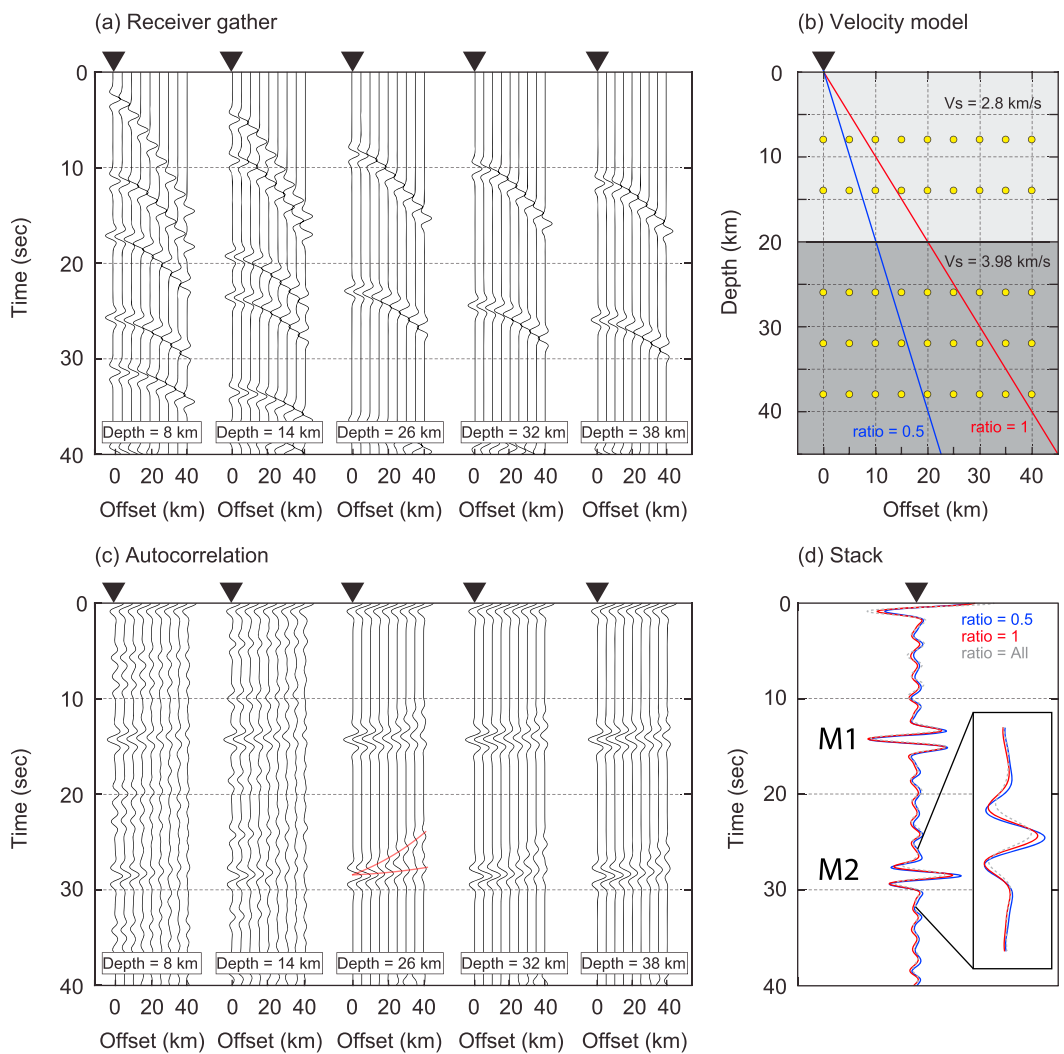


Figure 6. (a) The first 40 s of synthetic traces for sources within a simple, one-horizontal-layer velocity model (b). Total trace length is 100 s. After autocorrelation (c), traces are aligned on the direct arrival, effectively correcting for moveout of the direct arrival. Residual moveout remains for later arrivals after autocorrelation, since curvature of each reflector varies (c). However, the residual moveout is small compared to the wavelength of the data and arrivals stack constructively (d). A 0.5-Hz Ricker wavelet is used for the modeling, similar to the dominant frequency in our observed autocorrelation data. In autocorrelation trace (c), multiple phases arrive simultaneously with different moveout (red curves), and moveout corrections cannot optimally stack both arrivals. In our processing, we remove the initial moveout of the direct arrival via autocorrelation but do not correct for later moveout.

offsets to 45°. These autocorrelation traces at each station are linearly stacked to enhance coherent reverberations, primarily the surface multiples (Figure 4). The stacking also suppresses energy from phases with an arrival time dependent upon source depth (“depth phases”), which vary in time between events (Figure 5). The number of earthquake sources used per station stack ranged from 12 to 151 (Table S1).

As a test the same procedure is applied to background noise. For the noise processing, we extract data from 130 to 10 s before the P arrival for each earthquake. We follow all other processing steps used in the processing of the earthquake coda, although we stack all waveforms rather than inspect each trace.

4.1.1. Polarity of Autocorrelation Traces

Reflection coefficients vary as a function of incidence angle and material properties, and the sign of the coefficient may flip. For the range of incidence angles in our analysis, the reflection coefficient is negative for SH at any solid-solid boundary with a downward velocity increase (and positive for a velocity decrease) for geologically plausible wave speeds (Figure S2). Therefore, on SH data a velocity increase results in a negative

peak (Figure 5; or a positive peak for a velocity decrease). This is opposite the polarity of RFs, where a low impedance layer above a high impedance layer results in a positive peak. Thus, we reverse the polarity of the SH autocorrelation traces for consistency in display with RF results.

The procedure also removes polarity dependence on focal mechanism. That is because all upgoing rays from the source leave in a small range of the focal sphere and tend to have similar radiated amplitudes, as do all downgoing waves (though potentially flipped from upgoing rays). As a result, autocorrelation peaks corresponding to lags between two upgoing or between two downgoing raypaths all result in the same polarity on autocorrelation traces (Figure 5). Autocorrelation peaks corresponding to lags between upgoing and downgoing phases might have different polarities but because those phases arrive at times dependent on event depth, they stack out when multiple events are used (Figure 5c).

4.1.2. Pre-autocorrelation and Post-autocorrelation Filtering

We tested wide ranges of low- and high-pass limits for the filters (Figures S3–S10) and obtained optimal results using a preautocorrelation filter passband of 0.05 to 1.5 Hz, followed by a postautocorrelation and poststack band-pass filter of 0.6 to 1.5 Hz. Though the local earthquake signals include energy at 10 Hz (e.g., Figure 3), these frequencies are incoherent, likely from spatially aliasing over dipping structure at our station spacing of 10–15 km; coherent energy is in frequencies below 1 Hz (Figure S7, bottom row). Our postprocessing band-pass filter also removes a strong arrival at 10–12 s across the section (Figures S5–S7, upper rows). While the origin of this arrival cannot be established with certainty without further analysis, its persistence in the autocorrelations of ambient noise (Figures S11–S13) and its similarity across the whole array suggests that it is not related to structure in a simple way and is more likely either a filter effect or a characteristic of the ambient noise field. The autocorrelation filter transfer functions do not include a strong peak at 10–12 s (Figure S14), and prestack filtering above the microseismic noise peaks removes this arrival (by ~0.4 Hz; Figures S5–S7), allowing higher-frequency signals related to structure to dominate.

At the 0.6- to 1.5-Hz frequency band, signals have relatively low SNR (Figure 3); the use of these low SNR signals and the relationship between station spacing, frequency, and resolution is covered in the discussion. One-bit normalization of traces before autocorrelation is not required in our data set to see primary arrivals but enhances the phases and was thus applied in our processing flow.

4.1.3. Move-Out Corrections

We correct for the increase in time of the direct arrival as a function of earthquake-station distance (moveout) in the autocorrelation process, which aligns the direct arrivals at zero lag time across the full offset range. However, we do not correct for moveout of reverberations prior to stacking. The required time correction for each reverberation is unique, changing with each order of multiple (number of reverberations), and multiple reverberations from various layers and with differing order could arrive simultaneously with different curvature. Therefore, moveout corrections do not correctly adjust both primaries and multiple reverberations arriving at similar times. In standard active source processing, this feature of moveout corrections helps to suppress multiples that arrive simultaneously with primary reflections; however, we seek to keep both arrival types. Fortunately, the residual moveout on reverberations after alignment on the direct arrival is small compared to the wavelengths in our data (Figures 6 and S15), and the arrivals stack constructively without additional moveout corrections at either 22.5° or 45°. As an additional note, moveout corrections would require either clear arrivals from each boundary on a receiver gather or a priori knowledge of the depth and seismic velocities. In our receiver gathers, we do not see clear arrivals in prestack data (Figure S16).

4.1.4. Comparison of P, SV, and SH Component Results

The SH component stacks provide the most coherent images (Figure 7). The SV component stack also images the dominant structure (Figures S6–S8), but with weaker signals and increased constant-lag reverberations. The P component stack contains little coherent structure (Figures S9 and S10). The superior quality of the SH component stacks likely results from the following: (1) mode conversions arising from the interaction between P and SV in P and SV autocorrelations and (2) the lack of P-SV polarized Rayleigh wave energy in the ambient noise field on the transverse component, along with contributions from (3) the stability of the SH reflection coefficient as a function of angle and (4) the higher amplitude of shear waves than compressional waves. We therefore use the SH component for all interpretations and discussion and assume that arrivals are shear waves in all phase interpretations.

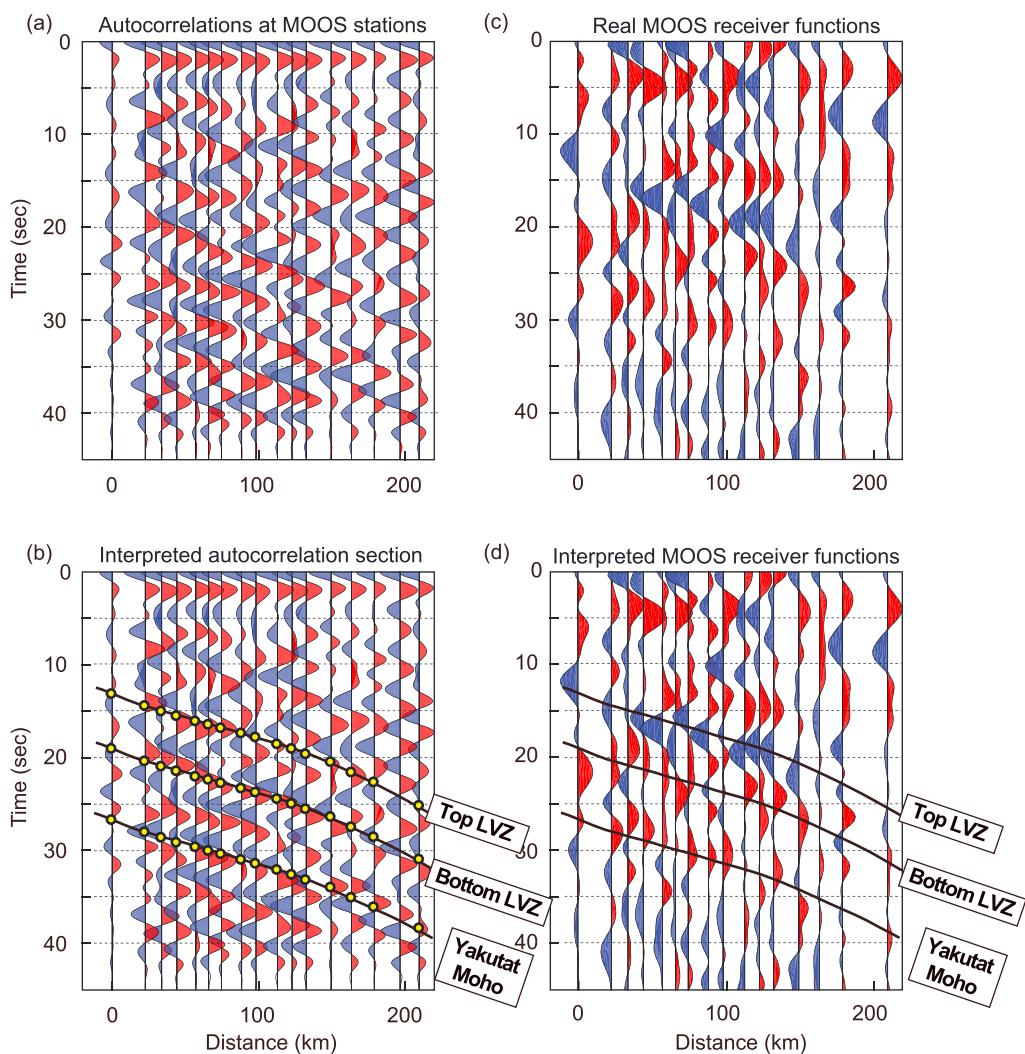


Figure 7. Comparison of the first 45 s of real autocorrelation traces and RFs. (a) Stacked SH component autocorrelation section from real data at MOOS stations, for events within a 22.5° cone beneath the station, and (b) interpreted autocorrelation stack. (c) Real RFs and (d) interpreted RFs at MOOS stations. Zero distance on section is from station HEAD (Figure 1). Yellow circles in (b) are the primary trough and peaks from the RF synthetic section in Figure 8d for comparison between sections. Note black lines represent expected arrivals and not necessarily clearly visible in each data type for each boundary. See Figure 10 and discussion in text in section 6.4 for the weaker match of the top of the LVZ shown in (b). MOOS = Multidisciplinary Observations Of Subduction; LVZ = low-velocity zone; RF = receiver function.

4.2. Synthetic Modeling

We use the SPECFEM2D code (Tromp et al., 2008) and available a priori structural information from earlier MOOS results (Kim et al., 2014; Li et al., 2013) to model synthetic local earthquake waveforms (Figures 8 and 9) from 38 model hypocentral locations, one above and one below the LVZ for each station (Figure 2). The input 2-D velocity model relies upon structural boundaries identified from the scattered wavefield imaging results of Kim et al. (2014), combined with the number of layers and velocities of each layer from the 1-D model of Li et al. (2013). We added a LVZ atop the subducting slab to the model of Li et al. (2013), present in results from RF modeling (Kim et al., 2014; Figure 2), using initial values in the layer for V_s (2.1 km/s), V_p/V_s (2.0, within the reported range of 1.9–2.3), and thickness of the LVZ (5 km) from Kim et al. (2014). For our final models, we adjusted these values slightly (V_s of 2.0 km/s; V_p/V_s of 2.0; LVZ thickness of 6 km) to achieve consistent arrival times for main phases between synthetic data, autocorrelation data, and RF data (also see section 5.2). We use the same processing steps as for the real data to generate synthetic autocorrelation traces and stack to create a synthetic record section (Figure 8) to compare to

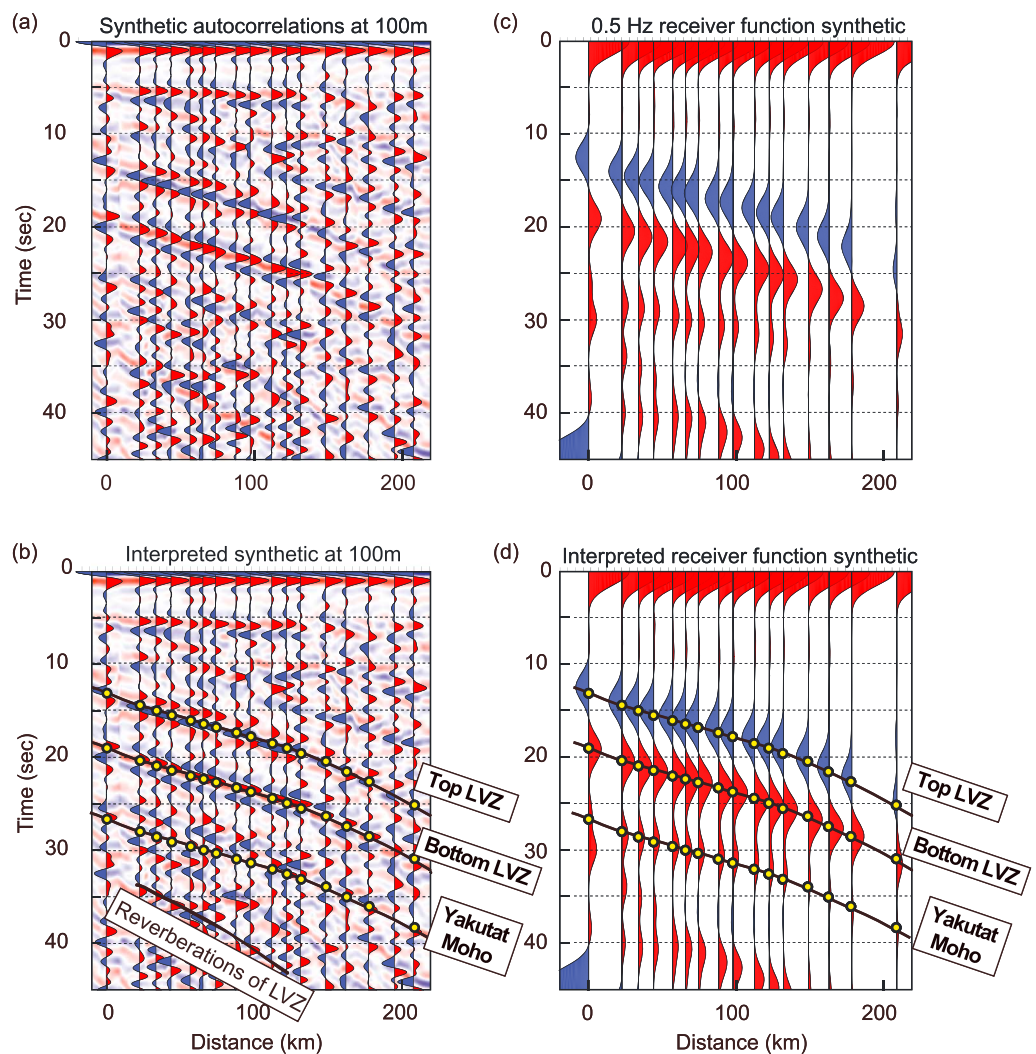


Figure 8. Comparison of the first 45 s of synthetic autocorrelation traces and synthetic RFs. (a) Synthetic autocorrelation section produced by SPECFEM2D (Tromp et al., 2008) at MOOS station locations using the modeled slab structure (Figure 2b), with synthetic data at idealized stations 100 m apart in the background, and (b) interpretation of the synthetic section. (c) Synthetic RFs at MOOS stations and (d) interpretation of the synthetic RFs. Zero distance on section is from station HEAD (Figure 1). Yellow circles in (b), and (d), are the primary trough and peaks from the RF synthetic section (c) for comparison between sections. LVZ = low-velocity zone; RF = receiver function; MOOS = Multidisciplinary Observations Of Subduction.

the observed autocorrelation sections along the transect. We also tested the effects of velocity variability within the LVZ using several additional velocity models, one with increasing velocity with depth within the LVZ, one with decreasing velocity with depth within the LVZ, and one with alternating velocity layers near the bottom of the LVZ (Figure 10).

Synthetic seismogram computations use a two-dimensional approximation of a double-couple moment tensor source ($M_{xx} = -1$; $M_{zz} = 1$; $M_{xz} = 0$; Tromp et al., 2008) and a Gaussian pulse with a central source frequency of 0.5 Hz to approximate the frequency spectrum of the filtered autocorrelation data. The grid spacing is ~1 km, with a model width of 309 km and depth of 110 km, and we use a time step of 0.002 s. The model is padded on either end of the transect by 40 km. To simulate realistic coda energy, we superimposed ~2 by 2-km scatterers with random, nonoverlapping locations within the crustal layer (Figure 2b). The scatterers each have a velocity perturbation randomly assigned of $\pm 1\%$ to $\pm 5\%$ of the P wave velocity, maintaining a constant V_p/V_s ratio. Synthetic data generated using our final model (Figures 9b and 9d) include the same phase arrivals as a model without scattering (Figures 9a and 9c),

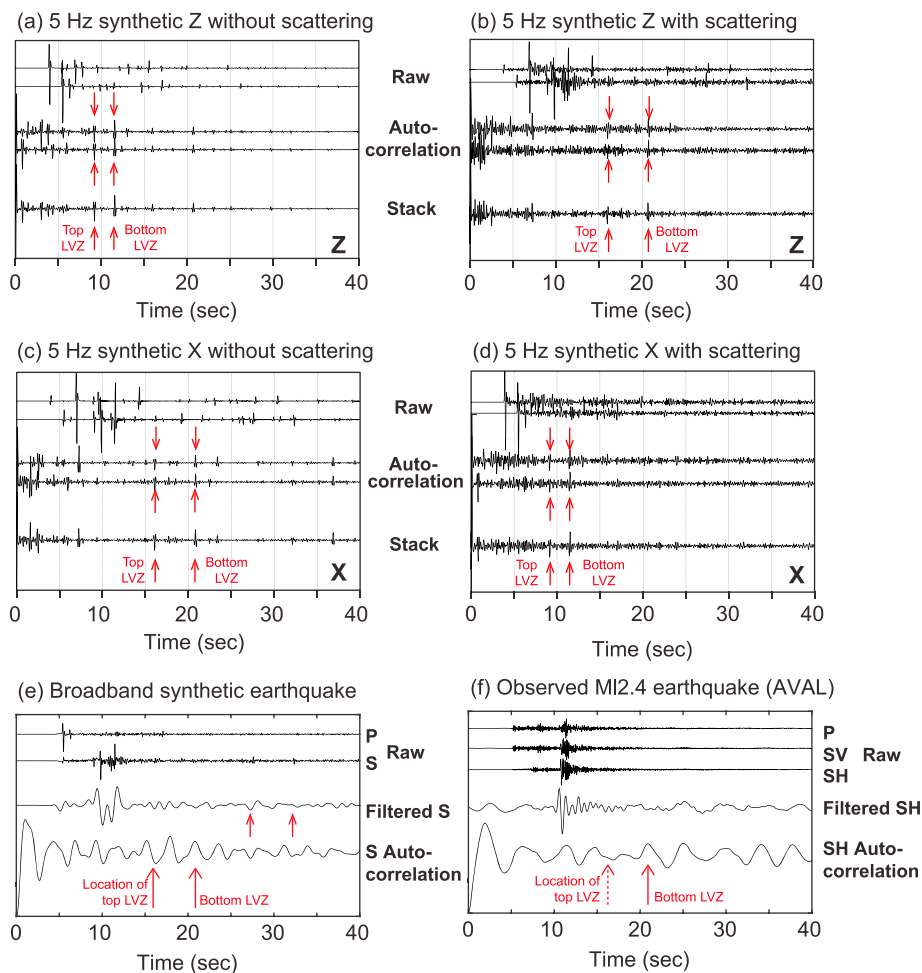


Figure 9. (a–d) High-frequency (5 Hz) SPECFEM2D synthetic waveforms with and without scatterers present in the velocity model. Distinct phase arrivals are visible in waveforms without scatterers, on both vertical (a) and horizontal (c) components, but arrivals are obscured by coda when scatterers are present (b, d). Surface multiples from the top and bottom of the LVZ (red arrows), are visible with or without scattering, are aligned by autocorrelation, and constructively stack for similar raypaths. Arrivals from the top and bottom of the LVZ arrive closer in time for compressional waves (a, b) than for shear waves (b, d). (e) SPECFEM2D synthetic waveforms, the SH filtered trace from 0.05 to 1.5 Hz as used in our autocorrelation processing and the resulting autocorrelation. f) Waveforms from an observed earthquake at station AVAL, the filtered SH trace (to 0.05–1.5 Hz), and its autocorrelation. In synthetic data (e), the top and bottom of the LVZ are visible arrivals. In the real data (f), the autocorrelation peak from the bottom of the LVZ is visible, but no clear phase is visible from the top of the LVZ. This is consistent with results from other earthquakes and other stations (see Figure 11). The velocity model used is in Figure 2b (without scatterers for a and b). LVZ = low-velocity zone.

but the arrivals with scattering are obscured by coda and less distinct. At frequencies comparable to those present in windows with local earthquakes, our synthetic data and autocorrelations (Figure 9e) are comparable to observed results (Figure 9f). Autocorrelation peaks are present in individual traces (Figures 9e and 9f) but difficult to interpret, similar to reflections in multichannel seismic data. Instead, coherent arrivals across multiple traces within a seismic section provide structural image (e.g., Figure 7).

In addition to the transect created using the actual station locations with 10- to 15-km spacing, we model hypothetical stations at 100-m spacing (Figure 11) to investigate the effects of station spacing on spatial aliasing and maximum usable frequency. These simulations test additional central frequencies of 1, 2, 5, and 10 Hz, decreasing the grid spacing to 100 m and the time step to 0.001 s. The size of the scatterers decreased with the central frequency such that the scatterer size was less than the dominant wavelength (e.g., Frankel & Clayton, 1986).

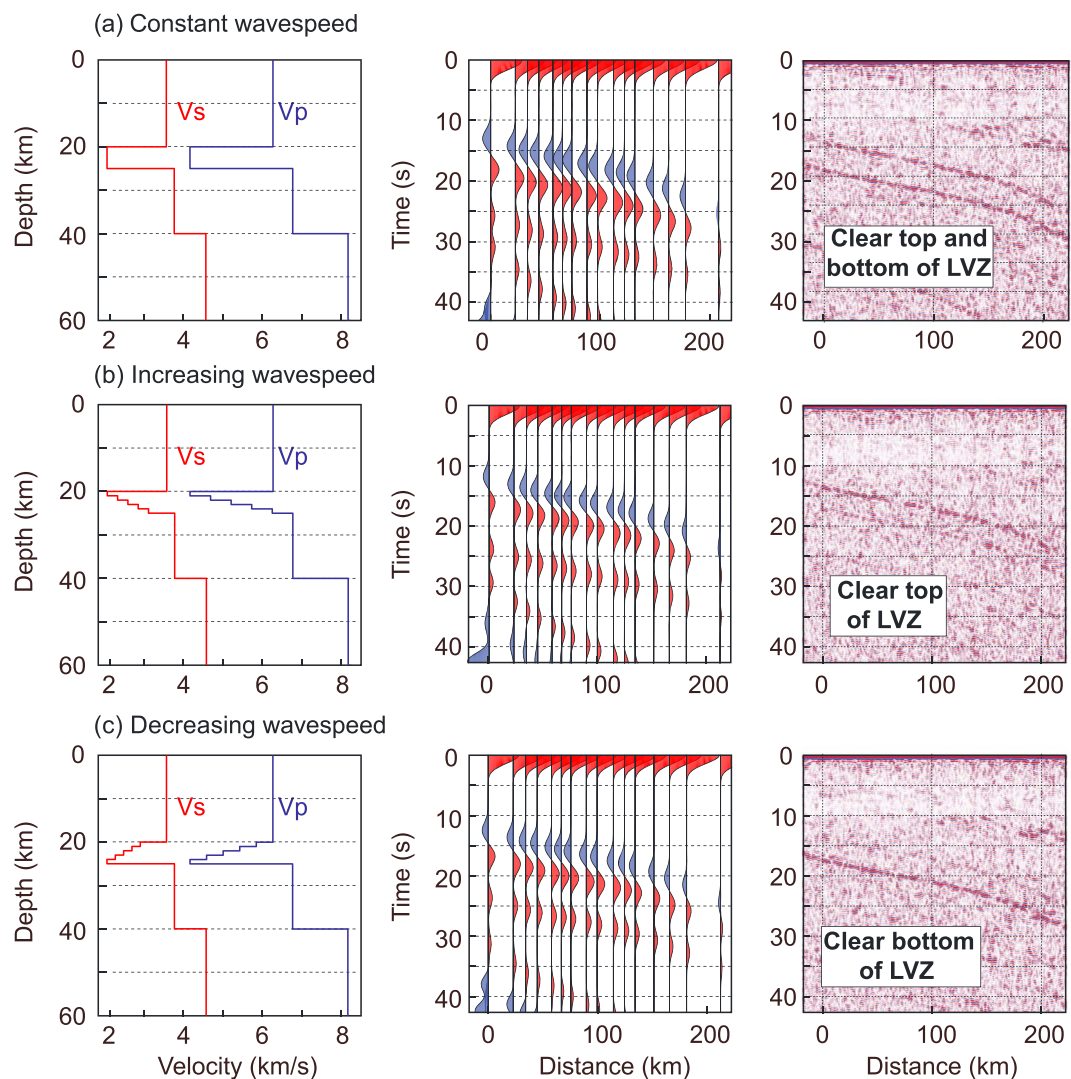


Figure 10. Models of possible LVZ structure, including (a) constant wave speed within the LVZ, (b) increasing wave speed from top to bottom within the LVZ, and (c) decreasing wave speed from top to bottom within the LVZ. Also included are RF (middle panel) and autocorrelation (right panel) synthetic data for each of these three velocity models. RF synthetic data include arrivals from the top and bottom of the LVZ for all three cases, however, in autocorrelation data, the strength of the top and bottom reflections of the LVZ are strongly dependent upon the velocity structure. The model of decreasing wave speed within the LVZ best matches the observed strong bottom reflector without a distinct top reflector in the real autocorrelation data (Figure 7a), suggesting that wave speed decreases within the LVZ toward the top of the subducting crust. LVZ = low-velocity zone; RF = receiver function.

4.3. Receiver Functions

To compare our new autocorrelation results to a standardized set of RFs, we reprocessed RFs from MOOS data. We computed radial RFs at each MOOS station along the transect initially using 80 teleseismic earthquakes, a greater number of earthquakes than previously published (Kim et al., 2014). Similar to Kim et al. we use an array-based deconvolution method, deconvolving a single estimated incident wavefield arriving at all stations in the array (Bostock & Rondenay, 1999). We visually inspect each RF, and choose those with high SNR and low energy on the transverse component after filtering 0.03–1.0 Hz. After this step, each station has 54–80 individual RFs. For each station, we stack all RFs from a back azimuthal range of 260–360° (the most common back azimuths), applying a phase-weighted stacking method (Schimmel & Paulsen, 1997) after outlier removal. Limiting the range in this way avoids smearing due to dipping structures. The

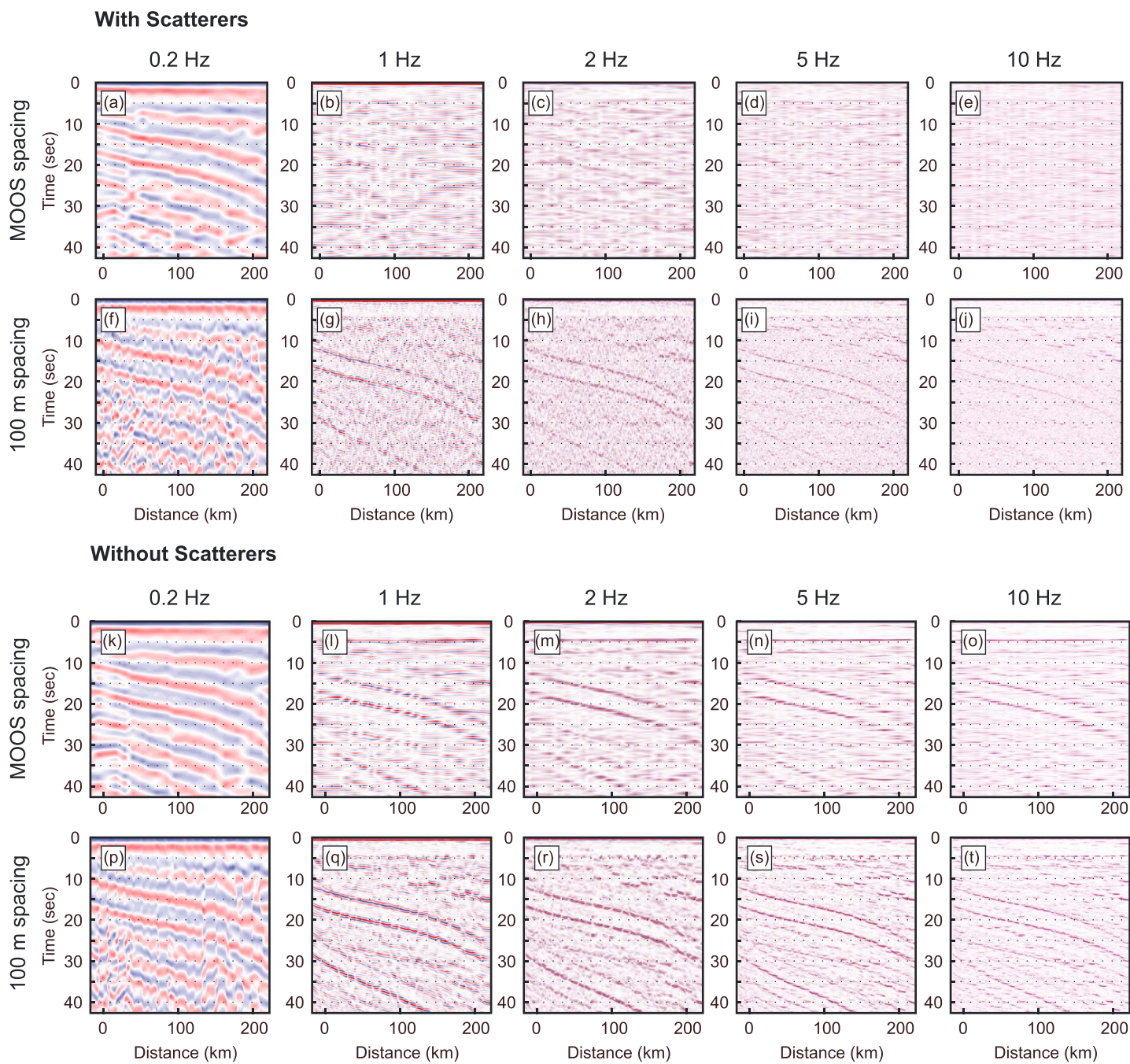


Figure 11. Comparison of synthetic SPECFEM autocorrelation sections at dense and sparse station spacing, with and without scatterers in the velocity model (Figure 2b) at different central frequencies. (a–e) Synthetic sections at the actual Multidisciplinary Observations Of Subduction (MOOS) station spacing of 10–15 km using dominant frequencies of 0.2, 1, 2, 5, and 10 Hz, respectively. (f–j) Synthetic sections at modeled 100-m station spacing. (k–t) Synthetic sections correspond to (a–j) but generated without scatterers in the model. Without scattering, slab structure can be retrieved at the MOOS station spacing, however, the structure is not imaged with scattering at 1 Hz at the MOOS station spacing. To recover such dipping structure at high frequencies, dense station spacing is required.

lag time in RFs corresponds to the lag time of the dominant phase (here, the S -to- P conversion); therefore, for comparison to autocorrelation data, we convert the lag time of each RF to an equivalent two-way S wave travel time (TWTT) for zero-offset sources (Figures 7 and 8). To do so, we use depth-averaged P and S velocities from our model and the average ray parameter for each RF stack, converting P -to- S RF lag time to S - S vertical incidence reflected time. With these conversions, we can directly compare signals in the RFs with

those in the autocorrelations, aligning boundaries with minimal alteration to a reference velocity model (see previous section). In particular, the background model is fixed and only the LVZ's V_s and thickness are adjusted slightly to achieve consistency between RF and autocorrelation arrivals.

As a test, we also adjusted the time to emphasize multiple reverberations within the 0.03- to 1-Hz filtered RFs, aligning arrivals from boundaries in the RF reverberations with the equivalent arrivals in the autocorrelation data (Figure S17b). This test explores the potential for higher resolution from RF multiples than direct conversions (Rondenay, 2009). Furthermore, we processed RFs using the same methodology as above but with a 0.03–0.3 band-pass filter (Figure S17c) and adjusted time to align reverberations with the equivalent autocorrelation arrivals to explore RF reverberations at lower frequencies (e.g., Tauzin et al., 2016). Because coherent arrivals are seen in multiples only at lower frequencies, no significant increase in resolution was obtained in our result (e.g., Rondenay et al., 2005).

We calculated synthetic RFs using a ray tracer that allows for planar dipping layers (Frederiksen & Bostock, 2000), using the local slab dip near each station from our model. The low-pass filter frequency and back azimuth of the modeled RFs are set to 0.5 Hz and 270°, respectively. Station KASH was particularly noisy for RF analysis due to the resonances within low-velocity sediments of the Susitna Basin (Kim et al., 2014) and removed from the final plot (Figure 7).

5. Results

5.1. Receiver Functions

The RFs do not vary significantly from prior results (e.g., Kim et al., 2014) but provide the benchmark for comparison with autocorrelation. The primary visible phase in the RF section, a negative trough, begins at ~12-s equivalent TWTT on the southern end of the line and increases to >26 s on the northern end. The trough is followed by a less distinct peak, from ~18 to ~32 s from south to north, and a later, weaker peak from ~26 to 30 s across the southern half of the section. Synthetic RFs and the migration image (Figure 2a) suggest that the negative phase corresponds to the top of a modeled LVZ (Figure 8d) and the following peak to the bottom of the LVZ. The second peak arrives at the expected time for a Moho arrival, based on the suggested thickness of Yakutat crust (Kim et al., 2014; Worthington et al., 2012). Our RFs use the same value of 1.0 Hz for a low-pass filter as our autocorrelation data; however, the spatial resolution of the RF is proportional to the one-way P - S differential time in the layer, significantly less than the TWTT for the shear wave in autocorrelation data. Hence, the RF wavelength for direct conversions is effectively longer than the wavelength for autocorrelation traces, even at the same frequency, and thus, direct conversions in RFs provide lower resolution. While reverberations on RFs may potentially increase the vertical resolution, such phases were not as strong or coherent in the reverberations filtered at the same frequencies for these northwest back azimuths (Figure S17b; Ferris et al., 2003). The phases are strong and coherent using a lower frequency bandpass of 0.03–0.3 Hz (Figure S17c; e.g., Tauzin et al., 2016), but the resolution of the reverberations at this lower-frequency range is similar to the direct conversions and again lower than that of autocorrelation results. Southerly back azimuths show greater evidence of the reverberations and potentially could provide higher resolution from RF data, although there are fewer and noisier signals. Ultimately, regardless of whether direct conversions or reverberations are used for RFs, the <1-Hz frequency band at which teleseismic P energy is dominantly present will ultimately limit resolution relative to higher-frequency local earthquakes used for autocorrelations, which could be pushed to higher frequencies if smaller station spacing were available (see section 6.5 below).

5.2. Autocorrelation of Local Earthquake Coda

On the SH autocorrelation stack, distinct and coherent phases appear across the full N-S section (Figure 7a), whether we restrict earthquakes to within 22.5° or 45° (Figure S18). Because of possible polarity reversals at wider angles (Figure 5), we use the 22.5° stack in our interpretations (Figures 7a and 7b). The first 2 s of the waveform are dominated by the autocorrelation zero lag arrival (a trough in the reverse-polarity stacked section) and its side lobe at 2 s. Strong, north dipping coherent arrivals are visible across the section starting after 15 s, beginning with a strong peak arriving at ~17 s on the southern end of the line and increasing in lag time to ~32 s at the northern end (Figures 7a and 7b). A second package of dipping arrivals begins at ~27 s on the southern end of the line, increasing to ~37 s over the first two thirds of the line before weakening (Figure 7a).

The dipping energy is similar in structure, arrival time, and polarity to dominant phases in the RFs and thus is a strong candidate for reverberations off of the subducting plate (Figure 7d). In particular, the arrival at 17–32 s has the same polarity and structure, and approximately the same arrival time, as the arrival from the bottom of the LVZ in the RFs, so we identify this autocorrelation arrival as the bottom of the LVZ. The V_p/V_s of the LVZ used in our model (2.0; Kim et al., 2014) did not require adjustment for alignment of the two data sets and is in the range reported from other studies of subduction systems (Audet et al., 2009; Hansen et al., 2012).

The later phase from 27 to 37 s resembles the expected arrival from the Moho of the subducting Yakutat crust based on active source imaging offshore (Christeson et al., 2010; Worthington et al., 2012) and in RFs further downdip (Ferris et al., 2003), though it is stronger in the real autocorrelation data than in the synthetic autocorrelation data (Figure 8a) or in the real RF data (Figure 7c). Unlike the arrival that corresponds to the expected arrival from the bottom of the LVZ, the negative phase visible in RFs from the top of the modeled LVZ is not distinct in the autocorrelation data; we discuss this difference in section 6.4.

The autocorrelation section based on preevent noise rather than earthquake coda (Figures S11–S13) is dominated by the constant-lag side lobe at 2 s and the ambient noise-related arrival at ~11 s. We suspect that this phase is related to the dominant 6- or 12-s Rayleigh wave microseisms, but a full analysis of noise characteristics is beyond the scope of this paper. The dipping phases observed in the local earthquake autocorrelation traces are not evident or are only weakly visible in the noise autocorrelation result.

5.3. Synthetic Autocorrelation

Our synthetic autocorrelation traces provide the seismic section that would be expected based on the SPECFEM2D modeled earthquake sources and the a priori structural model (Figure 2b; Kim et al., 2014; Li et al., 2013). The traces include reflections from the primary modeled boundaries, including the top and bottom of the LVZ and the bottom of the crust, and arrivals from peg-leg reverberations within layers (e.g., Figure 4).

On the SH component (Figure 8a), the autocorrelation zero lag and side lobes are visible, followed by a negative arrival from the top of the LVZ beginning at ~12 s of TWTT on the southern end of the transect and increase in time to ~27 s on the northern end of the line, where the slab is deeper. Arrivals from the bottom of the LVZ are also distinctly visible, as a peak, from ~18- to ~33-s TWTT from south to north. The phase at the predicted arrival time from the Moho of subducting crust is a weaker peak, arriving at ~27 s on the southern end and increasing to ~38 s on the northern end.

Energy arriving before the arrival from the top of the LVZ are partially caused by peg-leg arrivals within layers. Additionally, depth phases of each earthquake create arrivals at variable times depending on earthquake depth; the time shift associated with these depth phases will destructively interfere if enough earthquakes occurring at different depths are stacked together but are not fully suppressed. Of primary importance, each major interface in the a priori velocity model appears as an arrival in the synthetic autocorrelogram sections. Arrivals from the top and bottom of the LVZ are distinct in the model; the arrival from the base of the Yakutat crust is weak.

5.4. Velocity Model Variations

Our results differ most significantly at the top of the modeled LVZ; a strong signal is observed on RFs, but only an indistinct arrival is present in autocorrelation data, despite being predicted in synthetic data for a constant velocity LVZ. However, varying the velocity structure within the LVZ in synthetic models indicates that arrivals from the top and bottom of the LVZ in autocorrelation traces are strongly dependent upon the details of wave speed within the layer (Figure 10). For a model with constant velocity in the LVZ both the top and bottom interfaces are equally visible. However, a downward increasing or decreasing velocity within the layer results in only the top or bottom interface clearly visible, respectively (Figure 10). Alternating high- and low-velocity layers within the LVZ create ringing in the arrivals. A model with downward decreasing velocities in the LVZ and strong layering near its base best resembles the observed SH autocorrelograms. Details of the wave speed structure within the LVZ have little impact on modeled waveforms for RFs; the RF data are not sensitive to variability in this layer (Figure 10).

6. Discussion and Interpretation

6.1. Autocorrelation Imaging Using Earthquake Coda

The SH-polarized autocorrelation of local earthquake coda clearly images a distinct dipping boundary. The reflected phase from this boundary arrives at the expected reflected *S* wave arrival time of the bottom of the previously imaged LVZ (Figure 7a). A less distinct dipping phase coincides with the expected reflected *S* wave arrival from the bottom of the subducting Yakutat crust (Figure 7a). These primary arrivals correspond closely to arrivals visible in the RF image and synthetic autocorrelograms (Figures 7c and 7d, and 8a and 8b), providing confidence that the dipping arrivals are from primary structural boundaries of the subduction system. These arrivals best fit the expected arrivals on the southern end of the transect and diverge slightly from the expected time structure on the deeper, northern end. This is like an effect of not migrating the image, which results in a degraded image in the region of highest dip.

Missing in the autocorrelation image is a clear arrival from the top of the LVZ, which is a strong negative arrival on RF sections (Figure 7e). The absence of this boundary in the autocorrelograms may indicate complexities of this structure within the LVZ to which our autocorrelations are sensitive but below the resolution of the RFs. Waveform modeling of autocorrelation data indicates that a wave speed decrease with depth within the LVZ would result in a weak top and strong bottom arrival (Figure 10c) but that the same decrease would have little effect on RFs (Figure 10b). Although one would expect similar result from RFs, the higher resolution of the autocorrelation traces provides information on the nature of the subducting interface not previously available. We note that the bottom of the LVZ (positive corrected polarity) is clearer and more coherent in the autocorrelations than the RFs, which suggests some sort of wavelength-dependent complexity to the boundary reflectivity/transmissivity.

The bottom of the Yakutat crust is not a strong peak in autocorrelation data but appears to be more visible than in the RF image along this transect (Figure 7c; also Kim et al., 2014). The boundary is visible in RFs at greater depth and along a cross line (Ferris et al., 2003; Kim et al., 2014), perhaps indicating that geometry complicates imaging of this obliquely dipping surface, but that the geometry has less effect upon the autocorrelations.

6.2. SH Compared to *P* and SV Component Earthquake Data

In the *P* component autocorrelation section, no coherent dipping arrivals are visible (Figures S9 and S10), although such arrivals are expected based on synthetic models (Figure S19). On the SV component, dipping arrivals are present but with lower coherence than for the SH component and are dominated by constant-lag ringing in the first 10–15 s. The lower radiated *P* wave energy compared to *S* wave energy, and the resulting decrease in the amplitude of *P* wave reflections, may cause *P* wave energy to be insufficient to stack coherently above the noise. Additionally, for the *P* and SV components, recorded *P-SV* mode conversions interfere with *S* multiples. The amplitude of *P* and SV reflections are also more highly sensitive to incidence angle than SH reflections and flip polarity at modest incidence angles. The strong coherence of arrivals on the SH data compared to either SV or *P* is likely a result of the reduced mode converted energy on SH traces, the greater stability of amplitude for a range of incidence angles, and/or the lack of strongly periodic Rayleigh-wave-dominated microseisms.

6.3. Autocorrelation Imaging Using Ambient Noise Data

Autocorrelation imaging using the BHE, BHN, and BHZ components of background noise (Figure S11–S13) do not show clear dipping structure. Unlike the earthquake autocorrelation section, the noise autocorrelation sections show only the broad peak at ~10–12 s (Figure S11). This ringing is also visible on the local earthquake sections that have a low high-pass filter (e.g., Figure S3) but is removed using a high-pass filter of 0.6 Hz, above the microseism noise band. Although the frequency of data within noise windows is only slightly lower than frequencies preserved in the earthquake windows after the applied filters (Figure 3), the coherent energy of the earthquake signals is necessary to image deeper structure.

6.4. Interpretation of the Low-Velocity Zone

Low-velocity channels occur along the plate boundary at a number of subduction zones (e.g., Bostock, 2013). The LVZs might represent a high permeability and high fluid pressure channel. Estimates of high Poisson's ratios (high V_p/V_s) in LVZs support this idea (e.g., Audet & Schaeffer, 2018; Kato et al., 2010), as does the

inference that low effective stresses are necessary for slow slip events (e.g., Liu & Rice, 2007). Alternatively, the LVZs may reflect metamorphism of subducting sediments and altered crust along the plate boundary. Exhumed megathrusts are characterized by highly sheared metasedimentary rocks (e.g., Rowe et al., 2013), and seismic wave speeds within some LVZs are consistent with those of metasediments (Abers et al., 2009). Observations from southern Alaska provide two insights into this issue. First, the LVZ appears strong in our data throughout the region that ruptured in the great 1964 ($M_{W} 9.2$) earthquake (Figure 7), indicating that this feature is not confined to a downdip slow slip region (e.g., Audet & Schaeffer, 2018) but persists throughout the thrust zone. Evidence from other regions suggests only modest overpressures at seismogenic depths (Saffer & Tobin, 2011). Second, the observation that the bottom of the LVZ produces strong reflections but not the top indicates that the top of the channel does not have a sharp step in wave speed. High pore pressures confined to the LVZ would need to be bound by a strong permeability seal for them to be maintained at 20- to 40-km depth. Both of these observations suggest that in Alaska at least, the LVZ primarily represents a lithological channel, although a role for overpressure cannot be ruled out.

6.5. Implications for Dense Imaging Arrays: Synthetic Sections at Variable Spacing

Abundant high-frequency energy (>10 Hz) within local earthquake signals (Figure 3) would ideally be included in the autocorrelation imaging for highest resolution. However, in our results, inclusion of the high frequencies strongly degrades the coherency of the imaged structure (e.g., Figure S5), and we downfiltered to below 1.5 Hz. The loss of coherency with high-frequency data is likely related aliasing of the higher-frequency signals above dipping structures for sparse station spacing. In high-frequency synthetic data (to 10 Hz) with scattering in the upper crust (described in section 4.2), dipping reflectors are not imaged (Figure 11a) at the MOOS station spacing. A dense spacing is required to image the dipping structure (Figure S11e) in the presence of scattering. Without scattering, dipping structure can be retrieved even at the MOOS station spacing (Figure 11). Therefore, we conclude that a combination of dipping structure and seismic noise (including scattering) degrades the coherency of the higher frequencies in our real autocorrelation data. Horizontal boundaries remain visible at the MOOS station spacing, even when dipping structure is difficult to image (Figure S20). Either dense station spacing, to preserve unaliased data at high frequency, or alternatively a decrease in the dominant frequency can successfully retrieve dipping structures in noisy data.

A station spacing of ~1 km for signals at 4 km/s (S waves), or ~750 m for signals at 6 km/s (P waves), would preserve unaliased signals at 10 Hz over a layer dipping at 5° . These results should help to further motivate dense deployments.

6.6. Challenges in Using Autocorrelation Methods

Our autocorrelation results show strong coherence over dipping subduction boundaries. However, we also identified challenges in applying this method ubiquitously. In the Alaskan subduction system, earthquakes are comparatively abundant and well distributed, but we still needed to use a distance-to-depth ratio of 0.5 (a cone of $\sim 22.5^{\circ}$) to obtain reasonable raypaths. Hyperbolic moveout of the arrivals increases as this angle increases to include more earthquakes, creating challenges for stacking these arrivals particularly at higher frequencies. In principle, one should correct for moveout; however, many challenges remain before it can be implemented, including source location uncertainties, effects of velocity on ray angles, unknown structural dip, and simultaneous arrivals of multiple orders of reverberations. Additionally, the dip in this part of the Alaskan subduction system is low ($\sim 5^{\circ}$), making it possible for us to image the slab without migration and allowing greater station separation. Prestack migration methods that employ antialiasing (e.g., Biondi, 2001) or other dip corrections may be required for use of a similar method in areas of greater dip. We also note that the impedance contrast for the modeled LVZ is high compared to other impedance contrasts at this depth (e.g., for the Moho) and more subtle features may be harder to image. However, our results clearly show that reflected signals within local earthquake coda can coherently image crustal structure given an appropriate array and earthquake distribution.

7. Conclusions

We present seismic images of the subducting slab in the central Alaskan subduction zone using autocorrelation to extract scattered energy from local earthquake coda. Dipping interfaces of the subducting oceanic

plate are evident in our image and correlate to boundaries visible at lower resolution in our RFs. Our results suggest that *S* wave velocity decreases with depth toward the bottom of LVZ and is present throughout the thrust zone, favoring lithologic interpretations for the LVZ over ones purely dependent on excess pore pressure. Additionally, images show a clear Moho interface at the bottom of the subducting Yakutat crust that is not well imaged in RFs. Our result is thus one of the most compelling examples to date of using body waves within local earthquake coda (interferometry) to study plate structure. Our new images both provide information on the nature of the plate interface in the Alaska-Aleutian system and demonstrate the utility of using local earthquake coda for structural imaging in subduction zone with appropriate arrays. Because autocorrelations of local earthquakes are presently limited effectively by the station spacing of most networks, including in our study, denser networks would allow use of the full frequency range within local earthquakes and provide higher resolution to constrain small-scale structures. Autocorrelations of local earthquakes can thus theoretically achieve resolution beyond that possible using RFs, which are limited by the frequency content of arriving teleseismic waves. Autocorrelation imaging methodologies have the ability to produce higher-resolution images of deep structure than possible using other passive techniques, at much lower cost than active source multichannel studies.

Acknowledgments

This work was supported by NSF grant EAR-1347262. We acknowledge the thorough and thoughtful reviews of Dr. Benoit Tauzin and an anonymous reviewer that greatly improved the manuscript. Data in this manuscript are all available through the IRIS (Incorporated Research Institutions for Seismology) Data Management Center at network code YV. The synthetic waveforms are generated by SPECFEM2D (Tromp et al., 2008) and by Computer Programs in Seismology (Herrmann, 2013). Initial and final slab models, modeling input files, and numerical data produced by the models are available at <http://doi.org/10.7298/X43B5XD3>.

References

- Abers, G. A., MacKenzie, L. S., Rondenay, S., Zhang, Z., Wech, A. G., & Creager, K. C. (2009). Imaging the source region of Cascadia tremor and intermediate-depth earthquakes. *Geology*, 37(12), 1119–1122. <https://doi.org/10.1130/G30143A.1>
- Alaska Earthquake Center, Univ. of Alaska Fairbanks (1987). Alaska Regional Network, International Federation of Digital Seismograph Networks, Other/Seismic Network, 10.7914/SN/AK, <http://doi.org/10.7914/SN/AK>
- Audet, P., Bostock, M. G., Christensen, N. I., & Peacock, S. M. (2009). Seismic evidence for overpressured subducted oceanic crust and megathrust fault sealing. *Nature*, 457(7225), 76–78. <https://doi.org/10.1038/nature07650>
- Audet, P., & Schaeffer, A. J. (2018). Fluid pressure and shear zone development over the locked to slow slip region in Cascadia. *Science Advances*, 4(3), eaar2982.
- Biondi, B. (2001). Kirchhoff imaging beyond aliasing. *Geophysics*, 66(2), 654–666. <https://doi.org/10.1190/1.1444956>
- Bostock, M. G. (2013). The Moho in subduction zones. *Tectonophysics*, 609, 547–557. <https://doi.org/10.1016/j.tecto/2012.07.007>
- Bostock, M. G., & Rondenay, S. (1999). Migration of scattered teleseismic body waves. *Geophysical Journal International*, 137(3), 732–746. <https://doi.org/10.1046/j.1365-246x.1999.00813.x>
- Burdick, L. J., & Langston, C. A. (1977). Modeling crustal structure through the use of converted phases in teleseismic body-wave forms. *Bulletin of the Seismological Society of America*, 67(3), 677–691.
- Christeson, G. L., Gulick, S. P., van Avendonk, H. J., Worthington, L. L., Reece, R. S., & Pavlis, T. L. (2010). The Yakutat terrane: Dramatic change in crustal thickness across the Transition fault, Alaska. *Geology*, 38(10), 895–898. <https://doi.org/10.1130/G31170.1>
- Claerbout, J. F. (1968). Synthesis of a layered medium from its acoustic transmission response. *Geophysics*, 33(2), 264–269. <https://doi.org/10.1190/1.1439927>
- Dixon, T. H., & Moore, J. C. (2007). *The seismogenic zone of subduction thrust faults*. New York: Columbia University Press. <https://doi.org/10.7312/dixon13866>
- Draganov, D., Campman, X., Thorbecke, J., Verdel, A., & Wapenaar, K. (2009). Reflection images from ambient seismic noise. *Geophysics*, 74(5), A63–A67. <https://doi.org/10.1190/1.3193529>
- Ferris, A., Abers, G. A., Christensen, D. H., & Veenstra, E. (2003). High resolution image of the subducted Pacific (?) plate beneath central Alaska, 50–150 km depth. *Earth and Planetary Science Letters*, 214(3–4), 575–588. [https://doi.org/10.1016/S0012-821X\(03\)00403-5](https://doi.org/10.1016/S0012-821X(03)00403-5)
- Frankel, A., & Clayton, R. W. (1986). Finite difference simulations of seismic scattering: Implications for the propagation of short-period seismic waves in the crust and models of crustal heterogeneity. *Journal of Geophysical Research*, 91(B6), 6465–6489. <https://doi.org/10.1029/JB091iB06p06465>
- Frederiksen, A. W., & Bostock, M. G. (2000). Modelling teleseismic waves in dipping anisotropic structures. *Geophysical Journal International*, 141(2), 401–412. <https://doi.org/10.1046/j.1365-246x.2000.00090.x>
- Hansen, R. T. J., Bostock, M. G., & Christensen, N. I. (2012). Nature of the low velocity zone in Cascadia from receiver function waveform inversion, Earth planet. *Science Letters*, 337–338, 25–38.
- Herrmann, R. B. (2013). Computer programs in seismology: An evolving tool for instruction and research. *Seismological Research Letters*, 84(6), 1081–1088. <https://doi.org/10.1785/0220110096>
- Ichinose, G., Somerville, P., Thio, H. K., Graves, R., & O'Connell, D. (2007). Rupture process of the 1964 Prince William Sound, Alaska earthquake from the combined inversion of seismic, tsunami and geodetic data. *Journal of Geophysical Research*, 112, B07306. <https://doi.org/10.1029/2006JB004728>
- Ito, Y., & Shioi, K. (2012). Seismic scatterers within subducting slab revealed from ambient noise autocorrelation. *Geophysical Research Letters*, 39, L19303. <https://doi.org/10.1029/2012GL053321>
- Kato, A., Iidaka, T., Ikuta, R., Yoshida, Y., Katsumata, K., Iwasaki, T., et al. (2010). Variations of fluid pressure within the subducting oceanic crust and slow earthquakes. *Geophysical Research Letters*, 37, L14310. <https://doi.org/10.1029/2010GL043723>
- Kennett, B. L. N. (1991). The removal of free surface interactions from three-component seismograms. *Geophysical Journal International*, 104(1), 153–154. <https://doi.org/10.1111/j.1365-246X.1991.tb02501.x>
- Kim, D., Brown, L. D., Árnason, K., Ágústsson, K., & Blanck, H. (2017). Magma reflection imaging in Krafla, Iceland, using microearthquake sources. *Journal of Geophysical Research: Solid Earth*, 122, 5228–5242. <https://doi.org/10.1002/2016JB013809>
- Kim, Y., Abers, G. A., Li, J., Christensen, D., Calkins, J., & Rondenay, S. (2014). Alaska megathrust 2: Imaging the megathrust zone and Yakutat/Pacific plate interface in the Alaska subduction zone. *Journal of Geophysical Research: Solid Earth*, 119, 1924–1941. <https://doi.org/10.1002/2013JB010581>

- Li, J., Abers, G. A., Kim, Y., & Christensen, D. (2013). Alaska megathrust 1: Seismicity 43 years after the great 1964 Alaska megathrust earthquake. *Journal of Geophysical Research: Solid Earth*, *118*, 4861–4871. <https://doi.org/10.1002/jgrb.50358>
- Li, J., Shillington, D. J., Bécel, A., Nedimović, M. R., Webb, S. C., Saffer, D., et al. (2015). Downdip variations in seismic reflection character: Implications for fault structure and seismogenic behavior in the Alaska subduction zone. *Journal of Geophysical Research: Solid Earth*, *120*, 7883–7904. <https://doi.org/10.1002/2015JB012338>
- Lin, F.-C., Li, D., Clayton, R. W., & Hollis, D. (2013). High-resolution 3D shallow crustal structure in Long Beach, California: Application of ambient noise tomography on a dense seismic array. *Geophysics*, *78*(4), Q45–Q56. <https://doi.org/10.1190/geo2012-0453.1>
- Lin, F.-C., Moschetti, M. P., & Ritzwoller, M. H. (2008). Surface wave tomography of the western United States from ambient seismic noise: Rayleigh and Love wave phase velocity maps. *Geophysical Journal International*, *173*(1), 281–298. <https://doi.org/10.1111/j.1365-246X.2008.03720.x>
- Liu, Y. J., & Rice, J. R. (2007). Spontaneous and triggered aseismic deformation transients in a subduction fault model. *Journal of Geophysical Research*, *112*, B09404. <https://doi.org/10.1029/2007JB004930>
- MacKenzie, L. S., Abers, G. A., Rondenay, S., & Fischer, K. M. (2010). Imaging a steeply dipping subducting slab in southern Central America. *Earth and Planetary Science Letters*, *296*(3–4), 459–468. <https://doi.org/10.1016/j.epsl.2010.05.033>
- Nakata, N., Snieder, R., & Behm, M. (2014). Body-wave interferometry using regional earthquakes with multidimensional deconvolution after wavefield decomposition at free surface. *Geophysical Journal International*, *199*(2), 1125–1137. <https://doi.org/10.1093/gji/ggu316>
- Nishitsui, Y., Minato, S., Boulenger, B., Gomez, M., Wapenaar, K., & Draganov, D. (2016). Crustal-scale reflection imaging and interpretation by passive seismic interferometry using local earthquakes. *Interpretation*, *4*(3), SJ29–SJ53. <https://doi.org/10.1190/INT-2015-0226.1>
- Rondenay, S. (2009). Upper mantle imaging with array recordings of converted and scattered teleseismic waves. *Surveys in Geophysics*, *30*(4–5), 377–405. <https://doi.org/10.1007/s10712-009-9071-5>
- Rondenay, S., Bostock, M. G., & Fischer, K. M. (2005). *Multichannel inversion of scattered teleseismic body waves: Practical considerations and applicability*. *Geophysical Monograph* (Vol. 157, p. 187). Washington, DC: American Geophysical Union.
- Roux, P., Sabra, K. G., Gerstoft, P., Kuperman, W. A., & Fehler, M. C. (2005). P-waves from cross-correlation of seismic noise. *Geophysical Research Letters*, *32*, L19303. <https://doi.org/10.1029/2005GL023803>
- Rowe, C. D., Moore, J. C., Remitti, F., & Scientists, t. I. E. T. (2013). The thickness of subduction plate boundary faults from the seafloor into the seismogenic zone. *Geology*, *41*(9), 991–994. <https://doi.org/10.1130/G34556.1>
- Ruigrok, E., & Wapenaar, K. (2012). Global-phase seismic interferometry unveils P-wave reflectivity below the Himalayas and Tibet. *Geophysical Research Letters*, *39*, L11303. <https://doi.org/10.1029/2012GL051672>
- Ryberg, T. (2011). Body wave observations from cross-correlations of ambient seismic noise: A case study from the Karoo, RSA. *Geophysical Research Letters*, *38*, L13311. <https://doi.org/10.1029/2011GL047665>
- Saffer, D. M., & Tobin, H. J. (2011). Hydrogeology and mechanics of subduction zone forearcs: Fluid flow and pore pressure. *Annual Review of Earth and Planetary Sciences*, *39*(1), 157–186. <https://doi.org/10.1146/annurev-earth-040610-133408>
- Schimmel, M., & Paulssen, H. (1997). Noise reduction and detection of weak, coherent signals through phase-weighted stacks. *Geophysical Journal International*, *130*(2), 497–505. <https://doi.org/10.1111/j.1365-246X.1997.tb05664.x>
- Schuster, G. T. (2009). *Seismic interferometry* (Vol. 1). Cambridge: Cambridge University Press.
- Shapiro, N. M., Campillo, M., Stehly, L., & Ritzwoller, M. H. (2005). High-resolution surface-wave tomography from ambient seismic noise. *Science*, *307*(5715), 1615–1618. <https://doi.org/10.1126/science.1108339>
- Song, T.-R. A., Helmberger, D. V., Brudzinski, M. R., Clayton, R. W., Davis, P., Pérez-Campos, X., & Singh, S. K. (2009). Subducting slab ultra-slow velocity layer coincident with silent earthquakes in southern Mexico. *Science*, *324*(5926), 502–506. <https://doi.org/10.1126/science.1167595>
- Tauzin, B., Bodin, T., Debayle, E., Perrillat, J.-P., & Reynard, B. (2016). Multi-mode conversion imaging of the subducted Gorda and Juan de Fuca plates below the North American continent. *Earth and Planetary Science Letters*, *440*, 135–146. <https://doi.org/10.1016/j.epsl.2016.01.036>
- Tromp, J., Komatsch, D., & Liu, Q. (2008). Spectral-element and adjoint methods in seismology. *Communications in Computational Physics*, *3*(1), 1–32.
- Tsuji, Y., Nakajima, J., & Hasegawa, A. (2008). Tomographic evidence for hydrated oceanic crust of the Pacific slab beneath northeastern Japan: Implications for water transportation in subduction zones. *Geophysical Research Letters*, *35*, L14308. <https://doi.org/10.11029/12008GL034461>
- Wapenaar, K., Slob, E., & Snieder, R. (2008). Seismic and electromagnetic controlled-source interferometry in dissipative media. *Geophysical Prospecting*, *56*(3), 419–434. <https://doi.org/10.1111/j.1365-2478.2007.00686.x>
- Worthington, L. L., Van Avendonk, H. J., Gulick, S. P., Christeson, G. L., & Pavlis, T. L. (2012). Crustal structure of the Yakutat terrane and the evolution of subduction and collision in southern Alaska. *Journal of Geophysical Research*, *117*, B01102. <https://doi.org/10.1029/2011JB008493>
- Zhan, Z., Ni, S., Helmberger, D. V., & Clayton, R. W. (2010). Retrieval of Moho-reflected shear wave arrivals from ambient seismic noise. *Geophysical Journal International*, *182*(1), 408–420.